International Journal of Applied Ceramic Technology

RESEARCH ARTICLE OPEN ACCESS

Effect of Sintering Parameters on the Densification, Microstructure, and Mechanical Performance of ZrB_2–SiC Ceramics

Prakhar Jindal[1] | Iason Krinis[2] | Vera Popovich[2] | Hans Brouwer[2] | Jyoti Botchu[1] | Yinglu Tang[3]

[1]Space Systems Engineering, Faculty of Aerospace Engineering, TU Delft, the Netherlands | [2]Materials Science and Engineering, Faculty of Mechanical Engineering, TU Delft, the Netherlands | [3]Department of Aerospace Materials, Faculty of Aerospace Engineering, TU Delft, the Netherlands

Correspondence: Prakhar Jindal (p.jindal@tudelft.nl; prakharjindal@gmail.com)

Received: 17 November 2025 | **Revised:** 30 January 2026 | **Accepted:** 16 February 2026

Keywords: densification mechanisms | grain size and porosity | milling-induced phase evolution | spark plasma sintering (SPS) | ultra-high temperature ceramics (UHTCs) | ZrB_2–SiC composites

ABSTRACT

Zirconium diboride (ZrB_2)–silicon carbide (SiC) composites are promising candidates for ultra-high temperature applications, yet optimizing their densification and mechanical performance without sintering additives remains a challenge. This study systematically investigates the independent and combined effects of three critical spark plasma sintering (SPS) parameters, that is, temperature, applied pressure, and dwell time, on the densification behavior, microstructure, and mechanical properties of ZrB_2–20 vol% SiC composites. Building upon prior work on powder preparation effects (e.g., Tungsten Carbide (WC) vs. ZrO_2 milling), this research uniquely focuses on how precise control of sintering conditions alone can tailor final material characteristics. The results demonstrate that optimizing sintering parameters yields significant property enhancement, achieving a maximum relative density of 99.2% (at 2100°C, 65 MPa, 15 min) and peak flexural strength of 516 MPa (at 2000°C, 65 MPa, 60 min). Hardness and fracture toughness reached 17.08 GPa and 3.85 MPa $m^{1/2}$, respectively, under optimized conditions. Through detailed microstructural and performance analysis, this work explains the fundamental role of individual sintering parameters in governing densification kinetics and mechanical outcomes. The findings offer practical guidance for additive-free, energy-efficient processing of ZrB_2–SiC ceramics for advanced aerospace and thermal protection systems.

1 | Introduction

Ultra-high temperature ceramics (UHTCs) such as zirconium diboride (ZrB_2) and hafnium diboride (HfB_2) are distinguished by a unique combination of structural and chemical attributes. Defined by strong covalent bonding and an inherent hexagonal crystal structure, these materials exhibit exceptional properties including extremely high melting points (>3000°C), superior thermal conductivity, mechanical strength, and oxidation resistance [1], making them a cornerstone of materials science for extreme environments. It is these fundamental properties that make them suitable for operation in applications that must endure high temperatures, rapid thermal shocks, and significant mechanical loads. Over the past few decades, ceramic matrix composites such as carbon/carbon (C/C) and carbon/silicon carbide (C/SiC) have found widespread use in aerospace applications, particularly in rocket nozzles and thermal protection systems. However, they are prone to oxidative degradation. C/C composites begin to oxidize rapidly above 500°C unless protected, while C/SiC composites cannot sustain prolonged exposure beyond 1650°C due to the active oxidation of the SiC phase [2].

To overcome such limitations, UHTCs have attracted considerable attention. Among them, ZrB_2 offers practical advantages over HfB_2, including lower density, reduced cost, and better processability [3], making it a viable candidate for reusable hypersonic vehicles, nose caps, and propulsion components.

Despite these merits, monolithic ZrB_2 is constrained by low fracture toughness (K_{IC}) and limited high-temperature oxidation resistance [4]. The incorporation of SiC as a secondary phase, typically around 20 vol%, has been shown to significantly improve thermal stability, hardness, grain refinement, and crack deflection behavior [5]. However, densification of ZrB_2–SiC composites remain a significant challenge due to strong covalent bonding, low self-diffusion rates, and the presence of persistent oxide impurities such as ZrO_2 and B_2O_3 on particle surfaces [5]. Conventional sintering techniques often require temperatures exceeding 2000°C and extended dwell times, which can induce grain coarsening and compromise mechanical performance.

Spark plasma sintering (SPS) has emerged as a powerful alternative for consolidating UHTC systems. Through the application of pulsed electric current and uniaxial pressure, SPS enables rapid densification at reduced temperatures and shorter sintering cycles. This process minimizes grain growth while enhancing densification kinetics by facilitating particle rearrangement and improving mass transport via diffusion, joule heating, and localized plastic deformation mechanisms [6].

While prior studies have largely emphasized the influence of sintering additives, powder refinement, or compositional modifications, the role of fundamental SPS process parameters, namely, temperature, applied pressure, and dwell time, has not been systematically explored. Each of these parameters independently governs key aspects of sintering kinetics and microstructural development: temperature controls atomic diffusion and grain boundary mobility; pressure enhances driving forces for pore elimination and particle packing; and dwell time dictates the duration available for densification and grain coarsening. A thorough understanding of their isolated and combined effects is essential for achieving controlled microstructures and tailored properties in additive-free ZrB_2–SiC composites.

In our previous work [7], we established that the choice of milling media (WC vs. ZrO_2) fundamentally alters the surface chemistry and phase purity of the starting powders. However, that study focused on the static material properties under a single sintering regime. It remains unclear how these chemically distinct powders respond to the dynamic variations of SPS parameters. Specifically, the independent influence of temperature, pressure, and dwell time on the densification kinetics of contaminated (WC-milled) versus pure (ZrO_2-milled) powders has not been systematically decoupled. Understanding this sensitivity is critical, as we hypothesize that the optimal sintering window is not intrinsic to the ZrB_2–SiC system itself, but is heavily dependent on the processing history and resulting impurity levels.

Consequently, the present study conducts a comprehensive and systematic parametric investigation into the independent and synergistic effects of sintering temperature, applied pressure, and dwell time on the densification behavior, microstructure, and mechanical properties, namely, hardness, flexural strength (σ_f), and K_{IC}, of SPS-processed ZrB_2–20 vol% SiC composites. Two distinct powder preparation routes, involving high-energy WC milling and conventional ZrO_2 milling, are employed to evaluate the generality of observed trends. The results offer new insight into how precise control over sintering parameters can optimize the performance of additive-free UHTC composites for demanding aerospace, propulsion, and thermal protection applications.

2 | Materials and Methods

2.1 | Powder Preparation

ZrB_2 powder (99.5% purity, hexagonal phase, particle size ~5.5 μm, density 6.09 g/cm^3) and SiC powder (beta-phase, 99.8% purity, particle size ~0.62 μm, density 3.21 g/cm^3) were used as the starting materials. The powders were weighed carefully to maintain a ZrB_2:SiC volume ratio of 80:20. Two different ball milling methods were used for powder preparation. In the first method, the powders were mixed by conventional ball milling in a glass beaker using ZrO_2 balls and ethanol as the milling media for 48 h (labeled as ZSZ samples). In the second method, high-energy milling was performed using WC balls and a WC jar at 300 rpm for 10 h with isopropanol as the milling medium (labeled as ZSW samples). After milling, the powders were dried in an oven at 180°C for 12 h and sieved through a 100 μm mesh to break up any agglomerates. Both procedures are described in detail in our prior work [7] and are not repeated here for brevity.

To quantify the effectiveness of particle refinement and dispersion, particle size distribution measurements were conducted using a laser diffraction particle size analyzer (Malvern Mastersizer 3000). The median particle size (D_{50}) was determined to be approximately 0.7 μm for ZSW powders and 3.8 μm for ZSZ powders, confirming the enhanced fragmentation and mixing achieved through high-energy WC milling.

The particle morphology of the raw ZrB_2 and SiC powders, as well as the mixed powder blends obtained after both ZrO_2 and WC ball milling, was examined using scanning electron microscopy (SEM). Representative SEM micrographs are shown in Figure 1. ZrB_2 particles exhibited angular shapes with relatively broad size distribution (~5–7 μm), while the SiC particles were more spherical and significantly finer (~0.5–1 μm). The post-milling micrographs confirmed homogeneous distribution of SiC in the ZrB_2 matrix, with better dispersion observed in the WC-milled samples due to the more intensive mixing action.

2.2 | Spark Plasma Sintering

The dried powders were densified using a SPS system (FCT Systeme GmbH, MSE, TU Delft, the Netherlands), equipped with pulsed direct current and programmable control of pressure and temperature. A 30 mm inner-diameter graphite die was used, and the powders were compacted between graphite punches. To prevent sticking and ensure uniform pressure transfer, 0.5 mm thick graphite foils were inserted between the powder and die

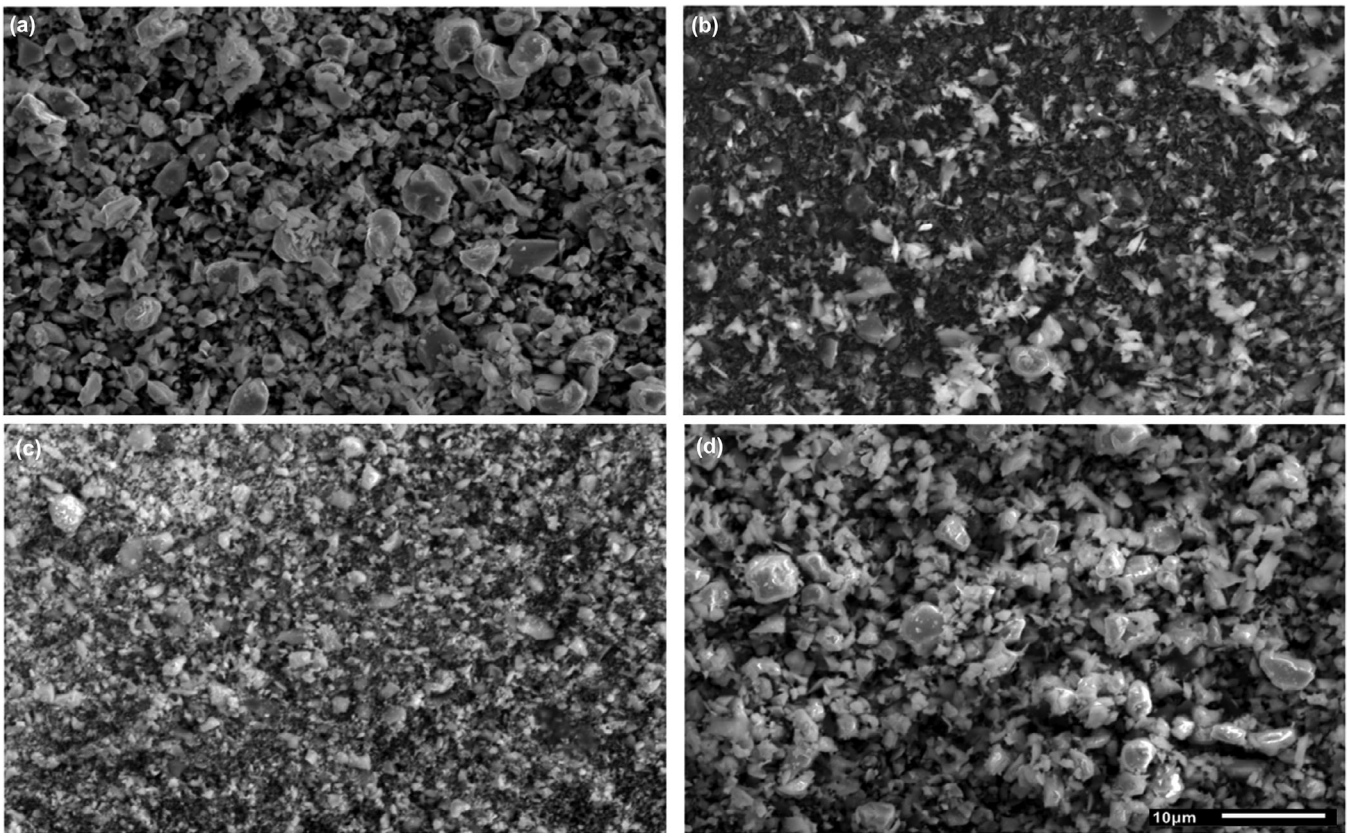

FIGURE 1 | SEM micrographs of (a) raw ZrB_2, (b) raw SiC, (c) ZSZ powder after ZrO_2 milling, and (d) ZSW powder after WC milling, all at 2000× magnification.

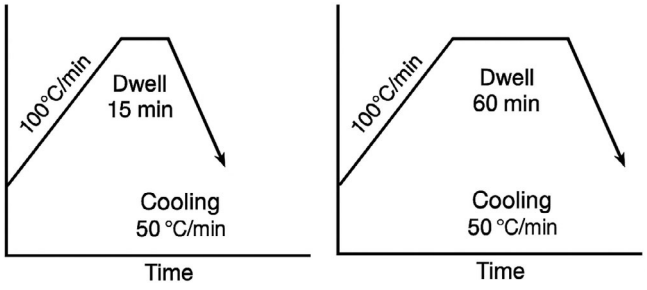

FIGURE 2 | Schematic representation of the sintering schedule followed in synthesizing ZrB_2–20SiC composite samples prepared through SPS technique.

walls and between the powder and punches. The die assembly was wrapped in a carbon blanket to reduce radial heat losses. All sintering was performed under a flowing argon atmosphere (~0.2 L/min) to prevent oxidation.

Samples were heated at a constant rate of 100°C/min to target temperatures ranging from 1950 to 2100°C, monitored using a thermocouple embedded in the graphite die wall near the sample. Pressure was applied uniaxially at two levels: 50 and 65 MPa. Holding times at maximum temperature were set at either 15 or 60 min. The pressure was maintained constant during the entire dwell period. A schematic representation of the sintering cycle is shown in Figure 2. The sintering parameters were selected to isolate the independent effects of temperature, pressure, and dwell time. Specifically, an extended dwell time of 60 min was included alongside the standard 15-min cycle to serve as a stress test for microstructural stability. This allows for the evaluation of whether prolonged diffusion drives beneficial defect healing in the milled powders or strictly detrimental grain coarsening. This approach enables a parametric investigation of their influence on densification and microstructure evolution, which is crucial for understanding SPS-related diffusion and mass transport mechanisms such as grain boundary sliding, viscous flow, and enhanced atomic diffusion under electric field effects.

After sintering, the pellets were approximately 30 mm in diameter and 3–5 mm in thickness. The naming convention for the samples reflects both the milling method and sintering parameters, as detailed in Table 1.

2.3 | Density Measurement

The density of the sintered samples was measured using the Archimedes method with distilled water as the immersion medium, following ASTM C373-88 [8]. At least five measurements were taken for each sample to ensure statistical reliability. Before testing, the samples were polished to remove any surface defects and dried thoroughly. The relative density (RD) was calculated by comparing the measured density to the theoretical density, as shown in Equation (1), which was determined based on the nominal densities of ZrB_2 and SiC and the expected volume

TABLE 1 | Sintering protocols and sample codes for ZrB_2–SiC composites.

Sample code	Milling method	Temperatur (°C)	Pressure (MPa)	Dwell time (min)
ZSW.1	WC milling	1950	50	15
ZSW.2	WC milling	2050	50	15
ZSW.3	WC milling	2000	65	15
ZSW.4	WC milling	2050	65	15
ZSW.5	WC milling	2100	65	15
ZSW.6	WC milling	2000	65	60
ZSW.7	WC milling	2100	65	60
ZSZ.1	ZrO_2 milling	1950	50	15
ZSZ.2	ZrO_2 milling	2050	50	15
ZSZ.3	ZrO_2 milling	2000	65	15
ZSZ.4	ZrO_2 milling	2050	65	15
ZSZ.5	ZrO_2 milling	2100	65	15
ZSZ.6	ZrO_2 milling	2000	65	60
ZSZ.7	ZrO_2 milling	2100	65	60

fractions.

$$\rho_{rel} = \frac{\rho_{exp}}{\rho_{theor}} \times 100 \quad (1)$$

where ρ_{exp} is the measured density and ρ_{theor} is the theoretical density, derived from the rule of mixtures based on the known volume fractions and densities of ZrB_2 and SiC.

2.4 | Microstructural Characterization

Polished cross-sections of the sintered specimens were analyzed using a digital optical microscope (Keyence VHX-5000) and a scanning electron microscope (JEOL JSM IT-100) equipped with secondary electron mode for enhanced topographical contrast. To ensure reproducibility and clarity in grain boundary detection, all specimens were etched thermally at ~1600°C for 10 min under inert conditions prior to SEM observation.

Grain size measurements were performed on high-contrast SEM micrographs of the thermally etched surfaces. For statistical reliability, at least 200 grains per sample were analyzed using the linear intercept method (ASTM E112 [9]). To accurately highlight and quantify porosity, a systematic image processing approach was employed using ImageJ software [10]. Initially, the SEM images were converted to grayscale to enhance contrast between the solid matrix and pore regions. Subsequently, thresholding techniques were applied to distinguish pores (appearing as darker regions) from the denser material. This process involved adjusting the grayscale histogram to isolate pixel intensity ranges corresponding to pores, effectively creating binary images where pores are represented distinctly. The software's "Analyze Particles" function enabled the measurement of pore areas, sizes, and distributions. By calculating the ratio of the total pore area to the overall image area, an estimation of surface porosity was obtained. This method aligns with established practices in materials characterization, as documented in literature sources [11, 12].

To support the optical observations, X-ray diffraction (XRD) analysis was performed using a Bruker D8 Advance diffractometer with Cu-Kα radiation ($\lambda = 1.5406$ Å) operated at 40 kV and 40 mA. A step size of 0.02° and scan speed of 1°/min were employed over a 2θ range of 20°–80°. A 0.5 mm beam slit was used to minimize peak broadening and improve resolution. The XRD data were analyzed to verify phase purity and the presence of any secondary or reaction phases, particularly ZrC, B_4C, or WO_3.

2.5 | Mechanical Properties Testing

The Vickers hardness (HV) of each sintered sample was measured using a DuraScan 20 microhardness tester (Struers) under a 1 kgf (9.81 N) load with a 15-s dwell time, in accordance with ASTM C1327-08 [13]. Sample surfaces were mirror-polished to remove surface irregularities. A minimum of five indentations were made at different locations on each sample, and average hardness was calculated using Equation (2):

$$HV = \frac{1.854.P}{d^2} \quad (2)$$

where P is load (N) and d is the average diagonal of the indent (mm).

σ_f was determined using a four-point bending test according to ASTM C1161-13 [14]standards. Sintered samples were cut and ground into bars with dimensions suitable for flexural testing (typically ~3 mm × 4 mm × 25 mm). The outer span was set to 20 mm, and the inner span to 10 mm. The surfaces of the flexural bars were ground and polished before testing to minimize surface flaws and avoid premature failure. Testing was conducted at room temperature using a Zwick Z010 mechanical testing machine with a crosshead speed of 0.2 mm/min. At least five bars were tested per condition, and σ_f was computed using Equation (3) as:

$$\sigma_f = \frac{3PL}{4bd^2} \quad (3)$$

where P is the breaking load (N), L is support span (mm), b is sample width (mm), and d is thickness (mm).

K_{IC} was estimated using the indentation fracture method with a 5 kgf (49.05 N) load and 15-s dwell time. Radial cracks from Vickers indents were imaged via SEM. Indents with $c/a > 2.5$ were considered valid for toughness calculations using the Halfpenny model [15, 16]. The K_{IC} is obtained using Equation (4).

$$K_{IC} = 0.0101.\frac{P}{\alpha.c^{1/2}} \quad (4)$$

where α is half indent diagonal and c is radial crack length from indent center. For each sintering condition, at least three samples were evaluated and five indents per sample were analyzed to ensure statistical reliability.

TABLE 2 | Summary of densification data and mechanical properties of the developed ZrB_2–SiC composites, spark plasma sintered with different milling methods.

SPS protocol	Sample	RD (%)	HV (GPa)	σ_f (MPa)	K_{IC} (MPa $m^{1/2}$)	Sample	RD (%)	HV (GPa)	σ_f (MPa)	K_{IC} (MPa $m^{1/2}$)
1950/50/15	ZSW.1	94.7	14.33±0.93	407±52	3.71±0.12	ZSZ.1	96.0	17.08±0.25	343±127	3.85±0.02
2050/50/15	ZSW.2	97.7	13.92±0.40	384±57	3.58±0.07	ZSZ.2	96.2	15.76±0.64	317±13	3.48±0.06
2000/65/15	ZSW.3	96.6	13.20±0.45	490±42	3.76±0.01	ZSZ.3	95.3	16.03±0.24	476±71	3.67±0.17
2050/65/15	ZSW.4	97.1	13.92±0.26	461±37	3.55±0.09	ZSZ.4	95.9	15.98±0.44	434±49	3.78±0.08
2100/65/15	ZSW.5	99.2	13.64±0.36	407±59	3.62±0.08	ZSZ.5	96.5	13.92±0.33	423±21	3.71±0.13
2000/65/60	ZSW.6	97.8	15.11±0.48	516±49	3.75±0.05	ZSZ.6	96.0	15.09±0.35	447±58	3.72±0.10
2100/65/60	ZSW.7	99.0	13.73±0.38	497±43	3.51±0.07	ZSZ.7	96.7	15.01±0.45	431±112	3.62±0.08

It should be noted that the Vickers indentation technique provides only an estimation of K_{IC} and may not fully capture stress-assisted toughening effects [17, 18].

3 | Results and Discussion

This section presents a systematic parametric analysis of how sintering temperature, applied pressure, and dwell time influence the densification behavior and mechanical performance of spark plasma sintered ZrB_2–SiC composites. To capture the independent effects of each parameter, the results are organized into three main subsections, each dedicated to one sintering variable, with property-specific subcategories, that is, RD, hardness, σ_f, K_{IC}. The results are presented in a comparative manner for both powder preparation routes, ZSW and ZSZ, allowing for clear evaluation of the influence of milling conditions in conjunction with the sintering parameters. Table 2 summarizes the complete set of experimental results, including RD, *HV*, σ_f, and K_{IC} for each sample, processed under different sintering protocols. This consolidated dataset forms the basis for all analyses and discussions in the following subsections.

3.1 | Effect of Temperature

Figures in this section present the variation in RD and mechanical properties of ZrB_2–SiC ceramics synthesized via two distinct powder processing routes, WC ball milling (ZSW) and ZrO_2 milling (ZSZ). These figures illustrate the effect of sintering temperature across three different constant sintering conditions: (i) 50 MPa, 15 min; (ii) 65 MPa, 15 min; and (iii) 65 MPa, 60 min. Within each condition, temperature was systematically varied to assess its influence.

3.1.1 | Relative Density

As seen in Figure 3(a), under the first sintering condition (50 MPa, 15 min), the ZSW samples exhibit a noticeable increase in RD from 94.7% at 1950°C to 97.7% at 2050°C, while the ZSZ samples show only a modest improvement from 96.0 to 96.2%. This suggests that temperature is a dominant densification driver for the ZSW route, likely due to finer particle size and improved packing achieved through high-energy milling. Under the second condition (65 MPa, 15 min), the ZSW RD increases from 96.6% at 2000°C to 99.2% at 2100°C, while the ZSZ samples rise from 95.3 to 96.5%. The enhanced densification at higher pressure indicates that both temperature and mechanical loading contribute synergistically to mass transport and pore closure, with a more pronounced effect observed in ZSW powders. In the third condition (65 MPa, 60 min), combining elevated pressure with prolonged dwell time, ZSW samples show densification from 97.8% at 2000°C to 99.0% at 2100°C, while ZSZ samples improve from 96.0 to 96.7%. These results suggest that extended sintering time promotes further diffusion-driven densification, especially for powders with higher initial homogeneity and surface activity. Across all conditions, ZSW samples consistently exhibit higher relative densities than their ZSZ counterparts, often approaching near-theoretical values. This advantage is attributed to a combination of factors introduced during WC ball milling: (i) finer particle size and narrower distribution leading to better initial packing, (ii) enhanced interparticle contact and dispersion of SiC within the matrix, and (iii) potential chemical effects from WC contamination that may locally reduce sintering resistance or promote transient liquid phase formation, thereby accelerating densification.

These trends align with prior studies by Fahrenholtz et al. [19], who reported that elevated sintering temperatures and pressures facilitate near-theoretical density in ZrB_2-based UHTCs, and Zhang et al. [20], who emphasized the role of dwell time in enhancing diffusion kinetics. The absence of anomalous behavior or irregularities across the dataset confirms the reliability of the sintering protocol. However, the relatively limited densification response of ZSZ samples under similar conditions suggests that powder packing inefficiencies and reduced surface activity associated with the ZrO_2 media may be contributing limiting factors.

3.1.2 | Hardness

As seen in Figure 3(b), the *HV* of the ceramics shows a complex dependency on sintering temperature and processing conditions. In the first condition (50 MPa, 15 min), both ZSW and ZSZ samples exhibit a decrease in hardness with increasing temperature. ZSW hardness reduces from 14.33 GPa at 1950°C to 13.92 GPa at 2050°C, while ZSZ samples show a more pronounced drop from 17.08 to 15.76 GPa over the same range. This reduction

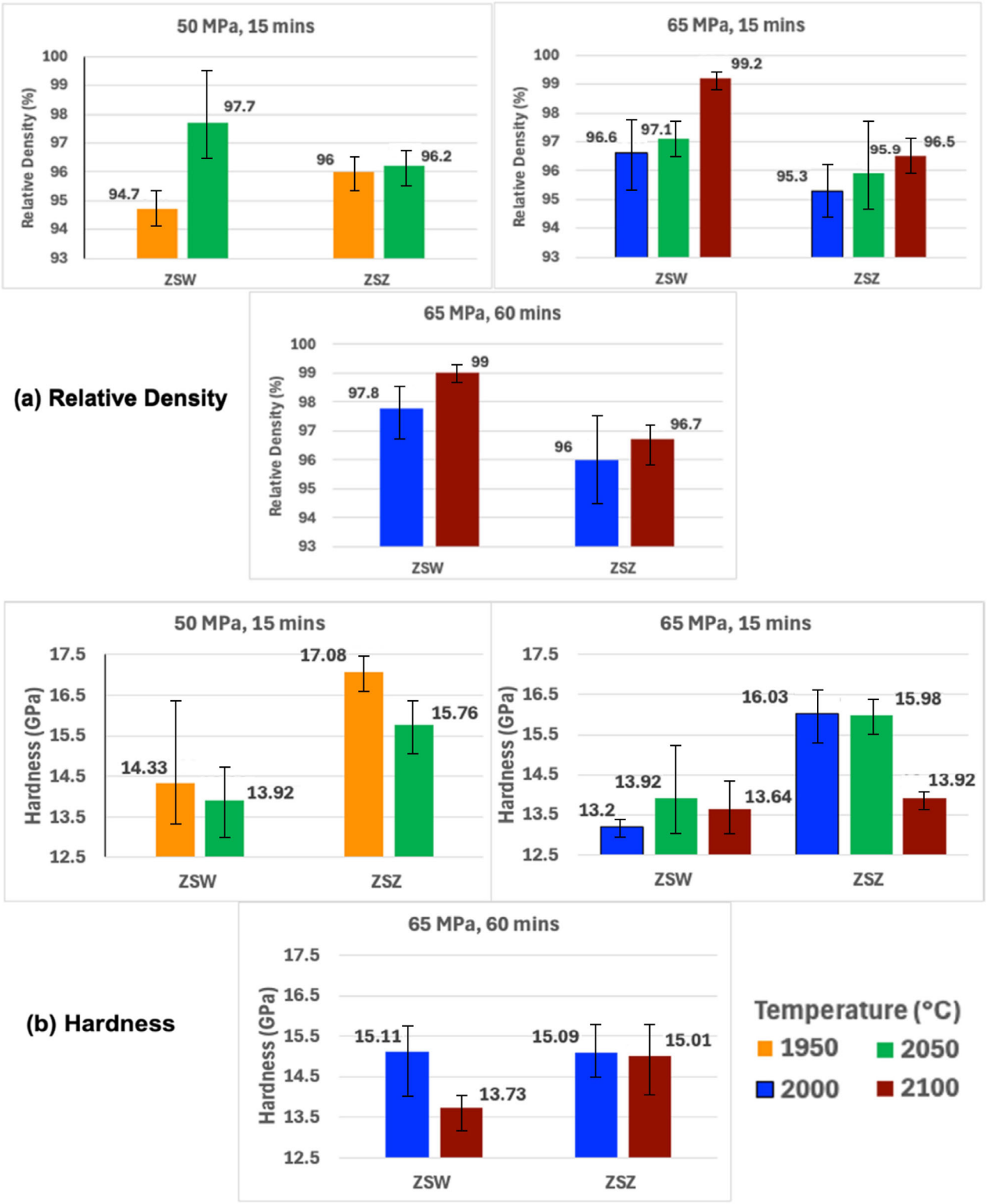

FIGURE 3 | Comparison of (a) relative densities and (b) hardness, between ZSW and ZSZ samples sintered at 50/65 MPa for 15/60 min, across various temperatures.

in hardness, despite improved densification (as seen in Section 3.1.1), is primarily attributed to thermally driven grain coarsening, which diminishes grain boundary strengthening effects (Hall–Petch relation), and potential thermal softening of the matrix or intergranular phases at elevated temperatures. The more significant drop for ZSZ suggests its microstructure might be more susceptible to high-temperature degradation, possibly due to a narrower window for optimal densification relative to grain growth.

Under the second condition (65 MPa, 15 min), the ZSW samples display a fluctuating hardness trend: an initial lower hardness

of 13.2 GPa at 2000°C, a slight recovery to 13.92 GPa at 2050°C, followed by a fall to 13.64 GPa at 2100°C. This behavior, despite the higher applied pressure and continued densification, indicates that concurrently occurring grain growth or other microstructural changes effectively counteract the benefits of increased density, leading to a complex interplay of strengthening and softening mechanisms. The ZSZ samples, conversely, peak at 16.03 GPa at 2000°C and then progressively decline to 13.92 GPa by 2100°C. This pronounced decline implies that increasing temperature beyond a specific threshold more significantly compromises ZSZ's mechanical rigidity, possibly due to more rapid grain growth or less stable grain boundaries in the absence of WC-related impurities.

The most notable behavior appears under the third condition (65 MPa, 60 min), where ZSW samples record an increase in hardness to 15.11 GPa at 2000°C, followed by a decline to 13.73 GPa at 2100°C. In contrast, ZSZ maintains relatively stable values of 15.09 GPa at 2000°C and 15.01 GPa at 2100°C. These results suggest that extended dwell time (60 min) provides a crucial period for microstructural stabilization in ZSW, partially compensating for the softening effects of high temperatures. This compensation is likely due to more uniform grain growth, optimal distribution of grains/secondary phases, or stress relaxation and healing of minor defects from prolonged thermal exposure, allowing the benefits of densification to translate more effectively into hardness.

In comparison with literature, similar temperature-induced softening trends have been reported in hot-pressed ZrB_2–SiC composites, where hardness values plateau or slightly reduce beyond optimal densification temperatures due to excessive grain growth or phase redistribution [21]. The consistently higher initial hardness of ZSZ samples (e.g., 17.08 vs. 14.33 GPa at 1950°C under 50 MPa, 15 min) likely stems from finer initial grain size retention and/or lower impurity levels resulting from the ZrO_2 milling process. Conversely, the hardness performance of ZSW, which often shows lower values despite achieving higher densities, improves significantly only when longer dwell times are applied. This suggests that the WC-induced secondary phases or the characteristics of WC-milled powders might initially hinder hardness by potentially forming softer phases or acting as stress concentrators, unless sufficient sintering time allows for optimal phase distribution, improved intergranular bonding, or healing of internal defects.

3.1.3 | Flexural Strength

Figure 4(a) illustrates the variation in σ_f of ZSW and ZSZ samples as a function of sintering temperature under the three different processing conditions. In all cases, the strength trend is closely related to densification efficiency and microstructural evolution, with key differences observed between the two powder processing routes. In the first condition (50 MPa, 15 min), ZSW samples show a decline in σ_f from 407 MPa at 1950°C to 384 MPa at 2050°C. ZSZ follows a similar trend, decreasing from 343 to 317 MPa.

This decrease, despite improved densification, is likely due to excessive grain growth or interfacial degradation at higher temperatures, which reduces crack deflection mechanisms and overall matrix cohesion. The limited dwell time may also restrict stress relaxation, resulting in higher residual stress accumulation that promotes early failure. Under the second condition (65 MPa, 15 min), both systems exhibit enhanced strength at 2000°C (ZSW rises to 490 MPa, and ZSZ to 476 MPa), likely due to improved particle rearrangement and stronger interfacial bonding driven by higher pressure. However, further heating to 2100°C causes both to decline again (ZSW to 407 MPa; ZSZ to 423 MPa), indicating a transition to over-sintering. This could stem from microcrack formation due to thermal mismatch between matrix and secondary phases, or grain boundary weakening from excessive growth.

The third condition (65 MPa, 60 min) shows the highest strength values. ZSW peaks at 516 MPa at 2000°C and drops only slightly to 497 MPa at 2100°C, while ZSZ increases to 447 MPa and then decreases to 431 MPa. This suggests that the prolonged dwell time provides sufficient diffusion for grain boundary healing and improved bonding, helping the material retain strength even at high temperatures. The higher strength of ZSW likely results from the more uniform and finer particle size distribution achieved by WC milling, which enhances initial packing, reduces pore formation, and supports stronger grain boundary integrity during sintering. All strength values reported here are the average of five individual bars tested per condition to ensure statistical reliability. These trends are consistent with literature on ZrB_2-based UHTCs, where maximum σ_f is typically observed at a balanced point between full densification and grain size control [19].

3.1.4 | Fracture Toughness

Figure 4(b) illustrates how sintering temperature influences the K_{IC} of ZrB_2–SiC composites under the three different sintering regimes. Across all conditions, the measured K_{IC} values fall within the expected range for nonadditive UHTCs, but subtle differences emerge based on processing history and thermal exposure. Under the 50 MPa, 15 min condition, ZSW exhibits a modest decline in toughness from 3.71 MPa $m^{1/2}$ at 1950°C to 3.58 MPa $m^{1/2}$ at 2050°C. ZSZ samples display a more pronounced drop from 3.85 to 3.48 MPa $m^{1/2}$ over the same range. Despite increasing density (see Section 3.1.1), this reduction in toughness is likely driven by thermally induced grain coarsening that weakens crack deflection mechanisms, as well as reduced internal compressive stress fields that would otherwise hinder crack propagation. The more significant decrease in ZSZ may be due to its faster grain growth kinetics or lower grain boundary strength, potentially linked to lower WC-induced pinning or phase effects.

At 65 MPa, 15 min, both compositions show more varied trends. ZSW initially improves to 3.76 MPa $m^{1/2}$ at 2000°C, then dips to 3.55 MPa $m^{1/2}$ at 2050°C before recovering slightly to 3.62 MPa $m^{1/2}$ at 2100°C. This fluctuation reflects a dynamic interplay between densification-enhanced bonding and grain growth-induced embrittlement. ZSZ peaks at 3.78 MPa $m^{1/2}$ at 2050°C before declining to 3.71 MPa $m^{1/2}$, a pattern similarly shaped by transient microstructural conditions. These results indicate that optimal toughness in this regime depends on striking a balance between full densification and the onset of coarsening or interfacial weakening. Under the third condition (65 MPa, 60 min), ZSW

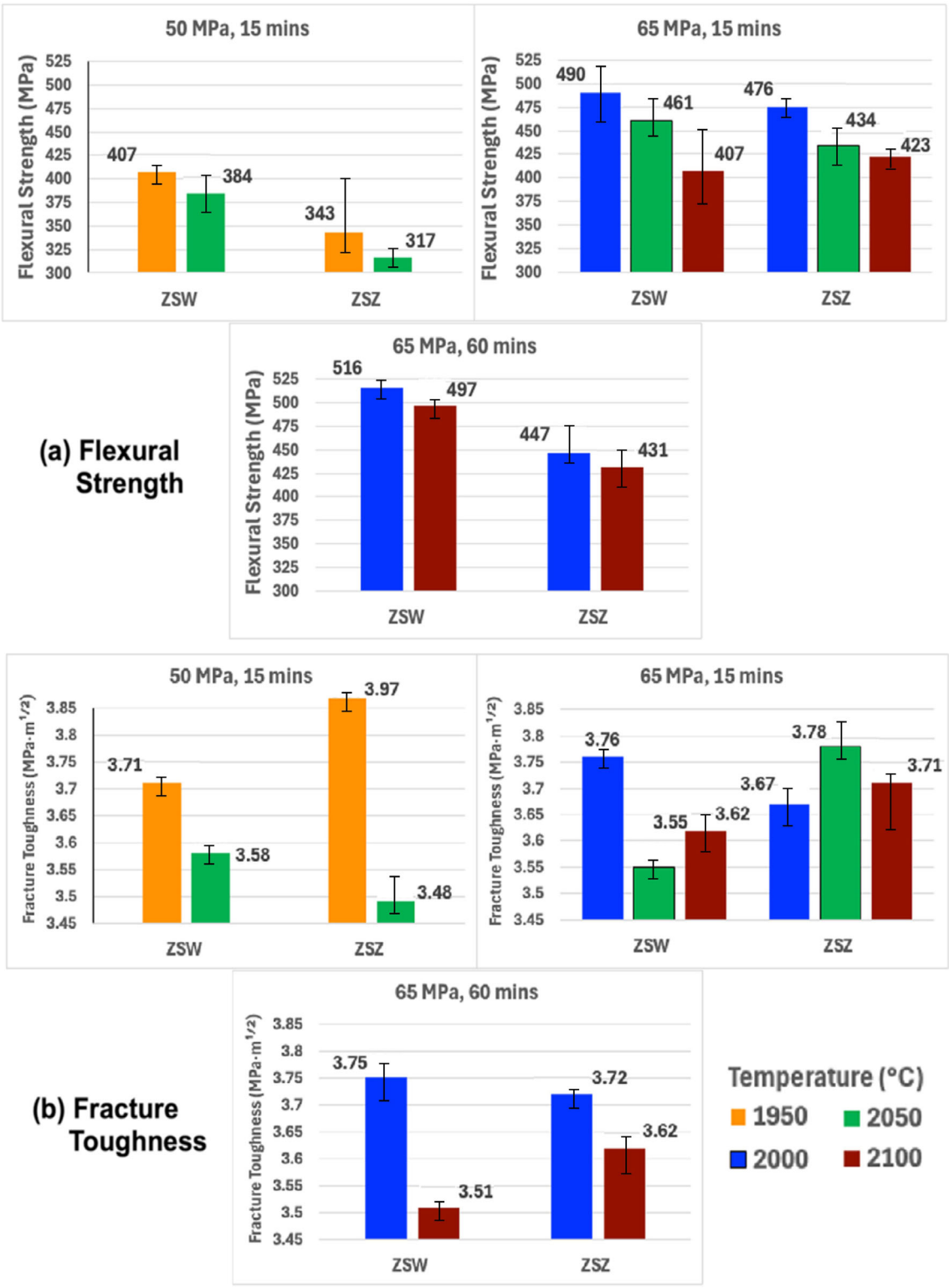

FIGURE 4 | (a) Flexural strength and (b) fracture toughness of ZSW and ZSZ samples as a function of sintering temperature at 50/65 MPa and 15/60 min dwell time.

and ZSZ exhibit more stable toughness behavior. At 2000°C, K_{IC} reaches 3.75 and 3.72 MPa $m^{1/2}$, respectively, with only a slight decrease to 3.51 and 3.62 MPa $m^{1/2}$ at 2100°C. The prolonged dwell time appears to promote microstructural homogenization and relaxation of thermal stresses, which helps maintain fracture resistance despite elevated temperatures. However, the minor reduction at 2100°C may still stem from intergranular phase redistribution or softening of second phases near the grain boundaries.

Notably, ZSZ consistently exhibits marginally higher K_{IC} than ZSW across most conditions, which may arise from finer grain

structures or cleaner grain boundaries due to the absence of WC contamination. WC-milled powders may introduce tungsten-rich secondary phases or induce microcrack precursors that modestly reduce toughness unless sintering conditions allow sufficient healing or redistribution. All K_{IC} values reported here are average results from at least five Vickers indentations per sample, across a minimum of three samples per condition. Only valid Palmqvist-type radial cracks with $c/a > 2.5$ were included in the calculations, ensuring statistical and methodological reliability.

These findings align with literature observations from Fahrenholtz et al. and Zhang et al. [19, 22], who emphasize that K_{IC} in ZrB_2-based composites is governed not solely by density but also by grain boundary characteristics, second-phase distribution, and microstructural uniformity. Therefore, optimizing sintering temperature for UHTCs must account not only for densification efficiency but also for preservation of the microstructure that enhances crack resistance.

3.2 | Effect of Pressure

This section investigates the isolated influence of applied uniaxial pressure on the densification behavior and mechanical properties of the ZrB_2–SiC composites. To effectively isolate the pressure effect, all samples in this section were sintered at a constant temperature of 2050°C and a dwell time of 15 min. These specific parameters were chosen as they represent conditions where significant densification was observed in Section 3.1, allowing for a clear assessment of how additional mechanical loading impacts the sintering process and final material properties at an already effective thermal and temporal state.

3.2.1 | Relative Density

Figure 5(a) evaluates the influence of applied uniaxial pressure on the RD of the ceramic composites, with both milling variants sintered at a constant temperature of 2050°C for 15 min. These parameters were selected to isolate the effect of pressure under conditions that previously yielded significant densification (see Section 3.1), thereby allowing a focused analysis of mechanical compaction on final microstructure. For ZSW samples, increasing pressure from 50 to 65 MPa results in a modest decrease in RD, from 97.7 to 97.1%. A similar but smaller reduction is observed in ZSZ samples, where density drops from 96.2 to 95.9%. This trend appears counterintuitive, as higher pressure is generally expected to enhance densification via improved particle rearrangement and pore collapse. However, the data suggest that near-saturation densification was already achieved at 50 MPa, rendering additional pressure less effective or even marginally detrimental under the fixed thermal and temporal conditions.

The slight decrease could also be attributed to microstructural effects induced during rapid sintering, such as localized overheating, grain boundary sliding, or the development of internal stresses that generate secondary porosity. For ZSW, interactions between WC contaminants and the ZrB_2–SiC matrix under higher pressure may contribute to subtle densification inefficiencies. Despite this, ZSW still achieves higher overall densities than ZSZ at both pressure levels, reaffirming the benefits of WC-based milling in promoting compact particle packing and diffusion kinetics.

These results contrast with conventional pressure-assisted sintering trends reported in literature [19], where densification generally improves with applied pressure, particularly in systems starting from lower initial densities. In this study, the already high initial relative densities (>96%) limit further densification gains. The behavior underscores the importance of considering powder-specific responses and the possibility of diminishing returns when pressure is applied beyond optimal thermal activation thresholds.

3.2.2 | Hardness

Figure 5(b) examines how applied pressure affects the *HV* of the composites at a fixed sintering temperature of 2050°C and dwell time of 15 min. For the ZSW samples, an increase in pressure from 50 to 65 MPa yields a marginal improvement in hardness, rising from 13.88 to 13.92 GPa. This limited change implies that the microstructure had already reached near-optimal densification and grain bonding at 50 MPa, with additional pressure offering negligible improvements. In contrast, ZSZ samples exhibit a more noticeable rise from 15.76 to 15.98 GPa, indicating a slightly stronger pressure dependence. This suggests that ZSZ responds better to higher compaction during sintering, possibly due to more uniform grain rearrangement or enhanced intergranular cohesion at elevated pressure. Notably, ZSZ maintains consistently higher hardness than ZSW at both pressure levels, a pattern that persists throughout the temperature and time regimes. This could be attributed to a combination of factors, including reduced contamination during ZrO_2 milling, better retention of fine grain structure, or lower formation of brittle secondary phases compared with the WC-milled ZSW. The limited effect of pressure on hardness, particularly in ZSW, may indicate that microstructural stagnation occurs once a critical grain configuration or pore elimination threshold is reached, and further mechanical compaction offers negligible benefits. Additionally, higher pressure may induce grain boundary sliding or thermal instabilities that offset any gain from improved densification. Prior studies on spark plasma sintered ZrB_2–SiC systems [21] show that the relationship between pressure and hardness becomes less linear at high relative densities, supporting this observation. The results also suggest that pressure alone is not a dominant factor in determining hardness once a baseline densification is achieved, particularly if sintering time and temperature are sufficient to promote complete phase bonding.

3.2.3 | Flexural Strength

Figure 5(c) investigates how the application of pressure influences the σ_f of the composites at a constant sintering temperature of 2050°C and a dwell time of 15 min. The results indicate a significant pressure-dependent increase in mechanical performance, particularly in both ZSW and ZSZ systems. For ZSW, σ_f improves from 384 MPa at 50 MPa to 461 MPa at 65 MPa, marking a substantial 20% enhancement. A similar trend is observed in ZSZ, which shows an even more pronounced rise from 317 to 434 MPa, an increase of nearly 37%.

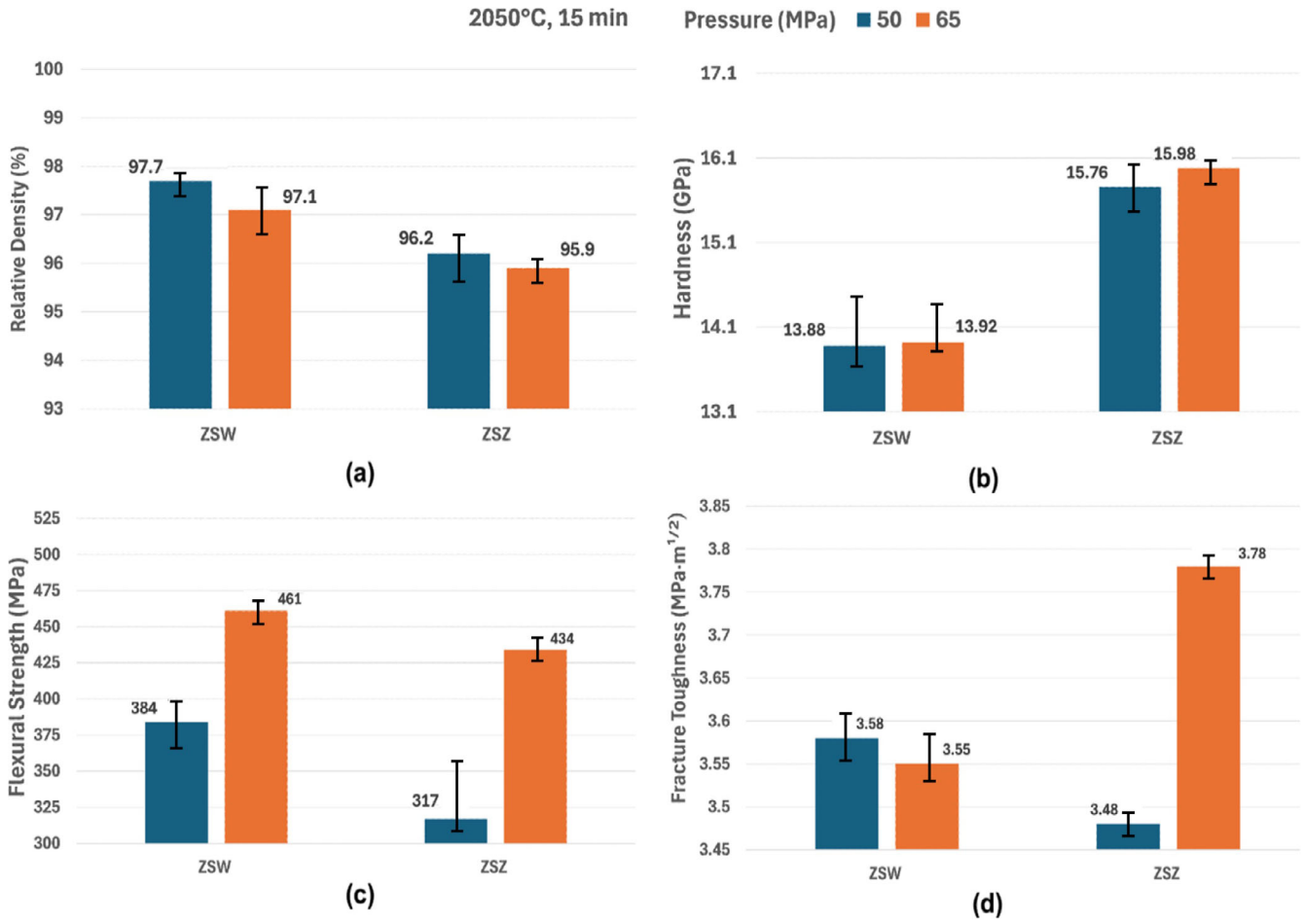

FIGURE 5 | Comparison of (a) relative density, (b) hardness, (c) flexural strength, and (d) fracture toughness, for ZSW and ZSZ samples sintered at 2050°C and 15 min under two pressure conditions.

These findings highlight the crucial role of applied pressure in enhancing mechanical robustness by facilitating improved particle rearrangement and pore elimination during the sintering process. Unlike RD and hardness, where the benefits of added pressure were either negligible or modest, the σ_f results reveal a much stronger sensitivity to mechanical compaction, likely due to the stress-distribution characteristics intrinsic to flexural loading. The pressure-induced improvements may be attributed to enhanced intergranular bonding and reduced flaw populations, which serve to delay crack initiation and propagation under load.

ZSW samples outperform ZSZ at both pressure levels, which is consistent with trends seen in the other mechanical property datasets and may be linked to better densification dynamics or favorable phase interactions arising from WC-based milling. However, the stronger response of ZSZ to pressure (i.e., greater relative increase) suggests that ZrO_2-milled powders benefit more from added mechanical force, possibly because they require higher pressure to overcome initial packing inefficiencies. Literature on pressure-assisted sintering of ZrB_2–SiC systems [22] supports this trend, emphasizing the importance of minimizing internal porosity and optimizing neck formation to achieve superior flexural performance.

3.2.4 | Fracture Toughness

Figure 5(d) presents the relationship between applied pressure and K_{IC} for the composites sintered at 2050°C for 15 min. For ZSW, toughness slightly decreases from 3.58 MPa $m^{1/2}$ at 50 MPa to 3.55 MPa $m^{1/2}$ at 65 MPa. This minor drop suggests that additional pressure may not benefit, or may even slightly degrade, crack resistance, possibly due to localized stresses or over-sintering effects that reduce energy-dissipating mechanisms like crack deflection or bridging. This aligns with earlier observations (Sections 3.2.1–3.2.3), where ZSW showed limited or negative responses to increased pressure, likely due to microstructural saturation or WC-induced heterogeneities.

In contrast, ZSZ shows a notable increase in K_{IC} from 3.48 to 3.78 MPa $m^{1/2}$, indicating a more favorable pressure-induced microstructural refinement. This enhancement may result from improved intergranular bonding or better grain boundary uniformity, which promote toughening mechanisms under load. Unlike ZSW, ZSZ appears to respond well to compaction, possibly due to cleaner grain interfaces and less contamination from milling media. These trends are consistent with the literature [20], which reports that K_{IC} in SPS-processed UHTCs depends heavily on microstructure quality and flaw population rather than

just density. Importantly, the observed divergence between ZSW and ZSZ reinforces that the effect of pressure is material-system dependent, influenced by factors such as particle morphology, milling-induced chemistry, and sintering path.

3.3 | Effect of Dwell Time

To isolate the influence of dwell time on the sintering behavior and mechanical properties of ZrB_2–SiC composites, experiments were conducted under a fixed pressure of 65 MPa at two sintering temperatures: 2000 and 2100°C. These temperatures were selected based on prior results where meaningful densification and mechanical variation were observed (Section 3.1), allowing a clear investigation into the temporal dynamics of sintering. While typical SPS cycles utilize short holding times (5–15 min) to minimize grain growth, this section examines the effect of prolonging the dwell time to 60 min. This extended duration was selected to determine if the defects and nonequilibrium interfaces introduced by high-energy milling require longer diffusion times to heal, or if the primary outcome is simply microstructural degradation due to coarsening. The results provide insight into the time–temperature coupling in SPS and help define optimal processing windows for both powder types.

3.3.1 | Relative Density

As shown in Figure 6(a), increasing the dwell time from 15 to 60 min enhances the RD of both ZSW and ZSZ at 2000°C. ZSW rises from 96.6 to 97.8%, and ZSZ from 95.3 to 96.0%, indicating improved atomic diffusion and pore elimination due to extended exposure. However, at 2100°C, ZSZ shows only a modest increase (96.5–96.7%), while ZSW slightly decreases (99.2–99.0%), implying that prolonged sintering may promote abnormal grain growth or phase boundary evolution that counteracts densification. These findings support the idea that dwell time is more effective when sintering kinetics are limited (lower temperature), but less critical or even detrimental once densification saturates under aggressive conditions. These interpretations are consistent with prior work by Zhang et al. [20], who reported diminishing returns in densification when dwell time was extended beyond the critical sintering point in fully reactive ZrB_2–SiC systems.

3.3.2 | Hardness

Figure 6(b) reveals that at 2000°C, ZSW hardness significantly increases from 13.2 to 15.11 GPa with longer dwell time, while ZSZ decreases from 16.03 to 15.09 GPa. The opposing trends suggest that ZSW benefits from enhanced bonding and porosity reduction, whereas ZSZ may suffer from grain coarsening or loss of dislocation barriers. At 2100°C, ZSW hardness shows a modest increase from 13.64 to 13.73 GPa as dwell time extends, while ZSZ shows a more noticeable rise from 13.92 to 15.01 GPa.

While Figure 6(a) indicates a slight reduction in ZSW RD at this temperature with extended dwell time, this marginal hardness improvement suggests that other microstructural refinements, such as subtle grain boundary healing or stress relaxation, may still occur, partially offsetting any negative impact from minor densification changes, or that the system is already near its maximum hardness potential.

These results indicate that ZSZ is more responsive to high-temperature diffusion when extended sintering is applied, whereas ZSW's microstructure stabilizes early. Overall, hardness trends reflect material-specific sensitivities to combined thermal and temporal inputs, in line with literature on ZrB_2–SiC UHTCs [21].

3.3.3 | Flexural Strength

As depicted in Figure 6(c), extending the dwell time improves ZSW strength from 490 to 516 MPa at 2000°C and from 407 to 497 MPa at 2100°C, suggesting that prolonged sintering enhances intergranular bonding and reduces flaw populations. ZSZ shows a decline from 476 to 447 MPa at 2000°C and a slight increase from 423 to 431 MPa at 2100°C, indicating a narrower processing window where excessive exposure can compromise mechanical integrity. These contrasting behaviors reflect the different sintering responses of each system and highlight the importance of tailored dwell times based on thermal sensitivity and initial powder characteristics. These findings are consistent with previous studies [22], which highlight that optimized dwell time at elevated temperatures is critical for developing maximum σ_f in ZrB_2–SiC systems. The overall results emphasize that the positive effects of dwell time are more pronounced in ZSW, likely due to delayed densification and higher sintering activation energy, while ZSZ exhibits a narrower process window before over-sintering effects become detrimental.

3.3.4 | Fracture Toughness

In Figure 6(d), K_{IC} remains nearly unchanged for ZSW (3.76 → 3.75 MPa $m^{1/2}$) and improves slightly for ZSZ (3.67 → 3.72 MPa $m^{1/2}$) at 2000°C. At 2100°C, both decrease modestly: ZSW from 3.62 to 3.51 MPa $m^{1/2}$, ZSZ from 3.71 to 3.62 MPa $m^{1/2}$. The mild degradation at higher temperatures with extended dwell is likely due to microstructural coarsening, which reduces toughening mechanisms like crack deflection or bridging. ZSZ consistently shows higher toughness, reinforcing the idea that ZrO_2 milling better preserves microstructural conditions favorable for fracture resistance. These trends reinforce the need to balance densification and grain evolution when optimizing dwell time, particularly in high-temperature sintering of UHTCs. These trends align with studies such as Zhang et al. [20], where toughness in ZrB_2–SiC ceramics was found to decline slightly beyond optimal sintering times, particularly at high temperatures.

3.4 | Morphology and Grain Size

3.4.1 | Microstructural Evidence of Densification: SEM Micrographs and Porosity Evaluation

To support the densification and mechanical trends discussed in Sections 3.1–3.3, Figure 7 presents processed SEM micrographs of the most porous (a) and least porous (b) samples, respectively. These images were analyzed using ImageJ software

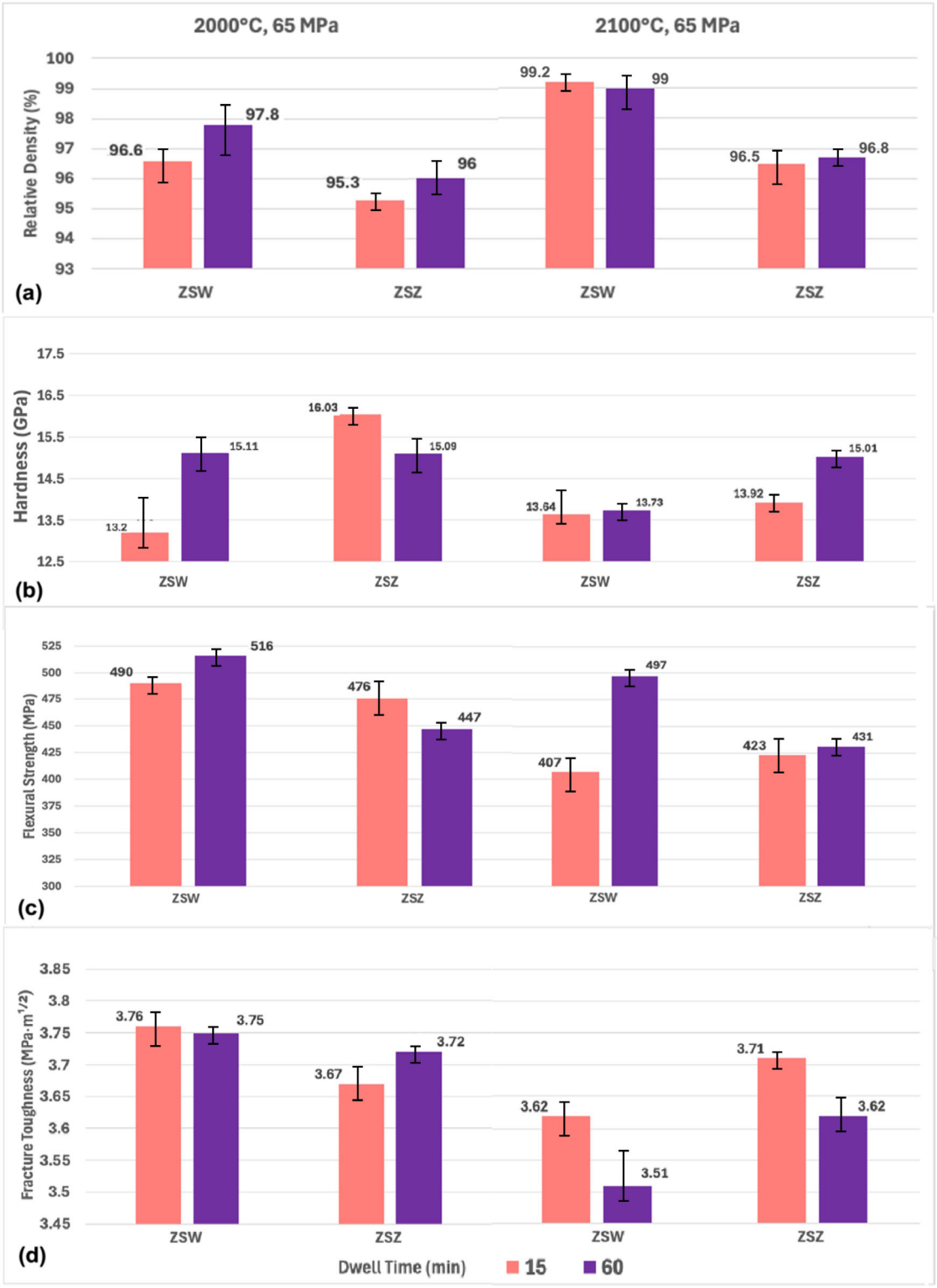

FIGURE 6 | Comparison of (a) relative density, (b) hardness, (c) flexural strength, and (d) fracture toughness, for ZSW and ZSZ samples sintered at 2050°C and 15 min, under two different pressures.

to quantitatively assess surface porosity, allowing visual confirmation of bulk density trends and better insight into pore morphology.

The corresponding ranking in Table 3 substantiates these visual findings, listing the samples in order of increasing porosity and providing the associated grain sizes for both ZrB_2 and SiC phases. Notably, the top-ranked ZSW samples (ranks 1–4) consistently exhibit low porosity (<2.5%) while maintaining controlled grain growth (~8–9 μm for ZrB_2). The ZSZ samples show more modest grain growth but higher porosity, suggesting less efficient densification despite smaller particle size.

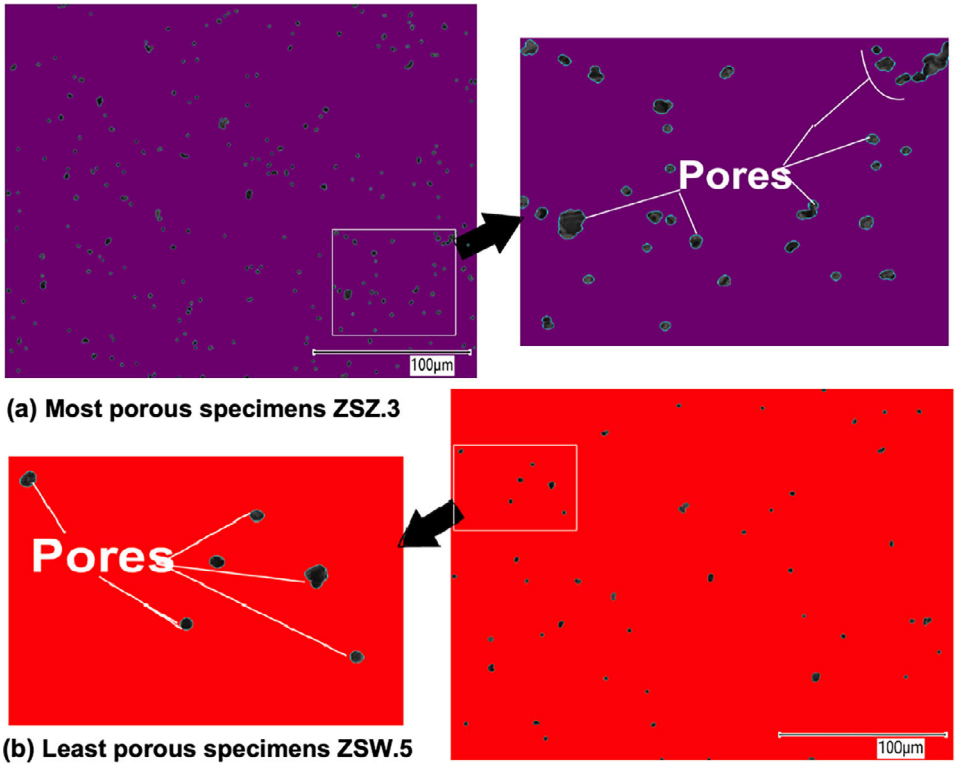

FIGURE 7 | Processed SEM micrograph highlighting the microstructural contrast in (a) most porous specimens ZSZ.3 and (b) least porous specimens ZSW.5.

TABLE 3 | Overall ranking of ZSW and ZSZ samples based on porosity, with corresponding grain sizes of ZrB_2 and SiC phases under different SPS condition (from least porous to most porous).

Rank	Sample	Temperature (°C)	Pressure (MPa)	Time (min)	Relative density (%)	Porosity (%)	Grain size (µm)	
							ZrB_2	SiC
1	ZSW5	2100	65	15	99.2	0.8	8.90 ± 0.46	3.03 ± 0.18
2	ZSW7	2100	65	60	99.0	1.0	9.18 ± 0.70	3.07 ± 0.27
3	ZSW6	2000	65	60	97.8	2.2	9.83 ± 0.37	3.07 ± 0.18
4	ZSW2	2050	50	15	97.7	2.3	8.13 ± 0.37	3.12 ± 0.18
9	ZSZ1	1950	50	15	96.0	4.0	9.03 ± 0.99	2.95 ± 0.21
10	ZSZ6	2000	65	60	96.0	4.0	8.40 ± 0.27	2.95 ± 0.15
11	ZSZ4	2050	65	15	95.9	4.1	8.91 ± 1.20	3.01 ± 0.26
12	ZSZ3	2000	65	15	95.3	4.7	8.82 ± 0.32	2.76 ± 0.15

Figure 7(a) corresponds to the ZSZ3 sample (2000°C, 65 MPa, 15 min), which exhibited the lowest RD (95.3%) and highest porosity (4.7%) as shown in Table 3. The processed SEM highlights a high density of irregular, intergranular pores. These are largely nonspherical, variably distributed, and lack connectivity, which is indicative of incomplete particle coalescence and early-stage sintering, particularly for ZrO_2-milled compositions under short dwell conditions.

Conversely, Figure 7(b) represents the ZSW5 sample (2100°C, 65 MPa, 15 min), which achieved a near-theoretical density of 99.2% and the lowest porosity (0.8%). The processed image shows an almost pore-free surface, with isolated small dark spots corresponding to residual porosity. Grain edges appear well defined and continuous, consistent with effective necking and interfacial diffusion driven by high thermal input and enhanced sintering kinetics due to WC-based milling.

While porosity percentages in Table 3 are calculated from bulk density, the ImageJ-based SEM analysis in Figure 7 offers a complementary, surface-level validation, revealing differences in pore shape, size, and distribution. These visual markers reinforce the role of sintering temperature, pressure, and powder processing in shaping the final microstructure and explain the disparities in mechanical performance observed earlier. In summary, the processed micrographs confirm that WC-milled ZSW compositions sintered at higher temperatures exhibit enhanced particle bonding and minimal surface porosity, while ZSZ samples under

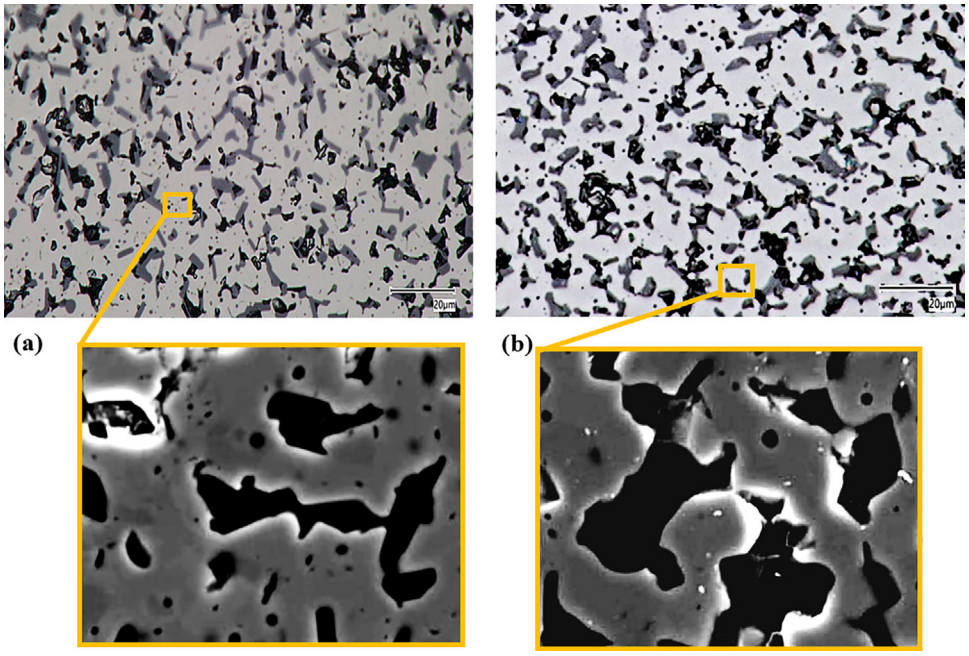

FIGURE 8 | High-contrast SEM micrographs of thermally etched surfaces (~1600°C, 10 min) for (a) the fully densified ZSW.5 specimen and (b) the porous ZSZ.3 specimen. The light gray matrix corresponds to ZrB_2 grains, while dark regions represent SiC particles and porosity. Insets show magnified regions with digitally traceable grain boundaries for grain size determination via the linear intercept method (ASTM E112).

lower thermal input display underdeveloped microstructures with persistent surface voids. This validates the quantitative ranking in Table 3 and supports the broader argument for carefully optimized sintering strategies.

3.4.2 | Grain Size versus Sintering Parameters

The evolution of grain size in ZrB_2–SiC composites as a function of sintering temperature and time was evaluated through SEM-based image analysis, with results summarized in Table 3 and visualized in Figures 8 and 9. Grain size measurements were performed using the line-intercept method (ASTM E112 [9]) on thermally etched SEM micrographs, with ZrB_2 appearing as lighter, angular grains and SiC as darker, intergranular regions. Grain pull-out zones (black areas) were excluded from analysis using ImageJ pixel–micron calibration.

As shown in Figure 8, microstructural contrast between the densest (ZSW.5) and most porous (ZSZ.3) specimens highlights the role of porosity and grain connectivity. ZSW.5, with only 0.8% porosity, exhibits relatively compact and equiaxed ZrB_2 grains (8.90 μm) and well-distributed SiC (3.03 μm), promoting effective load transfer and mechanical integrity. In contrast, ZSZ.3 (porosity 4.7%) shows signs of grain pull-out and coarser ZrB_2 grains (8.82 μm), yet achieves higher σ_f than expected, possibly due to local homogeneity or SiC phase interlocking.

Figure 9(a) displays the grain size distribution for all studied samples. ZrB_2 grain size ranges from 8.13 to 9.83 μm, with growth closely tied to sintering parameters. The coarsest grains are found in ZSW.6 (9.83 μm, 2000°C, 60 min), indicating that prolonged exposure, even at moderate temperature, can drive excessive coarsening. In contrast, SiC grains remain relatively stable across all regimes (2.76–3.12 μm), consistent with their known grain-boundary pinning effect and sluggish diffusion kinetics.

Figure 9(b), a multiaxis scatter plot, further illustrates the correlation between temperature and ZrB_2 grain growth, with dwell time acting as a secondary modulator. For example, ZSW.2 (2050°C, 15 min) maintains finer grains than ZSW.6, despite higher pressure and longer time in the latter. This confirms that temperature is the primary driver of coarsening, while longer sintering duration fine-tunes the process depending on the material system and milling history.

Notably, ZSW samples consistently exhibit coarser ZrB_2 grains compared with ZSZ under similar conditions, likely due to enhanced diffusion pathways introduced by WC contamination during milling. This promotes neck growth and particle coalescence. On the other hand, ZSZ samples maintain finer grains, benefitting from ZrO_2-mediated cleaner boundaries and reduced mass transport. The link between microstructure and mechanical performance is evident. Samples like ZSW.6 with coarsened ZrB_2 grains demonstrate slightly reduced K_{IC}, while those with finer grains and lower porosity, such as ZSW.5 or ZSZ.6, strike a better balance between strength, hardness, and crack resistance. These findings reinforce that optimal grain size control, especially for the dominant ZrB_2 phase, is essential for tailoring mechanical behavior in UHTCs.

3.4.3 | Phase Composition and Distribution Analysis

To understand the correlation between porosity, densification, and phase stability, XRD analysis was performed on two representative specimens with extreme porosities: ZSZ.3 (the most

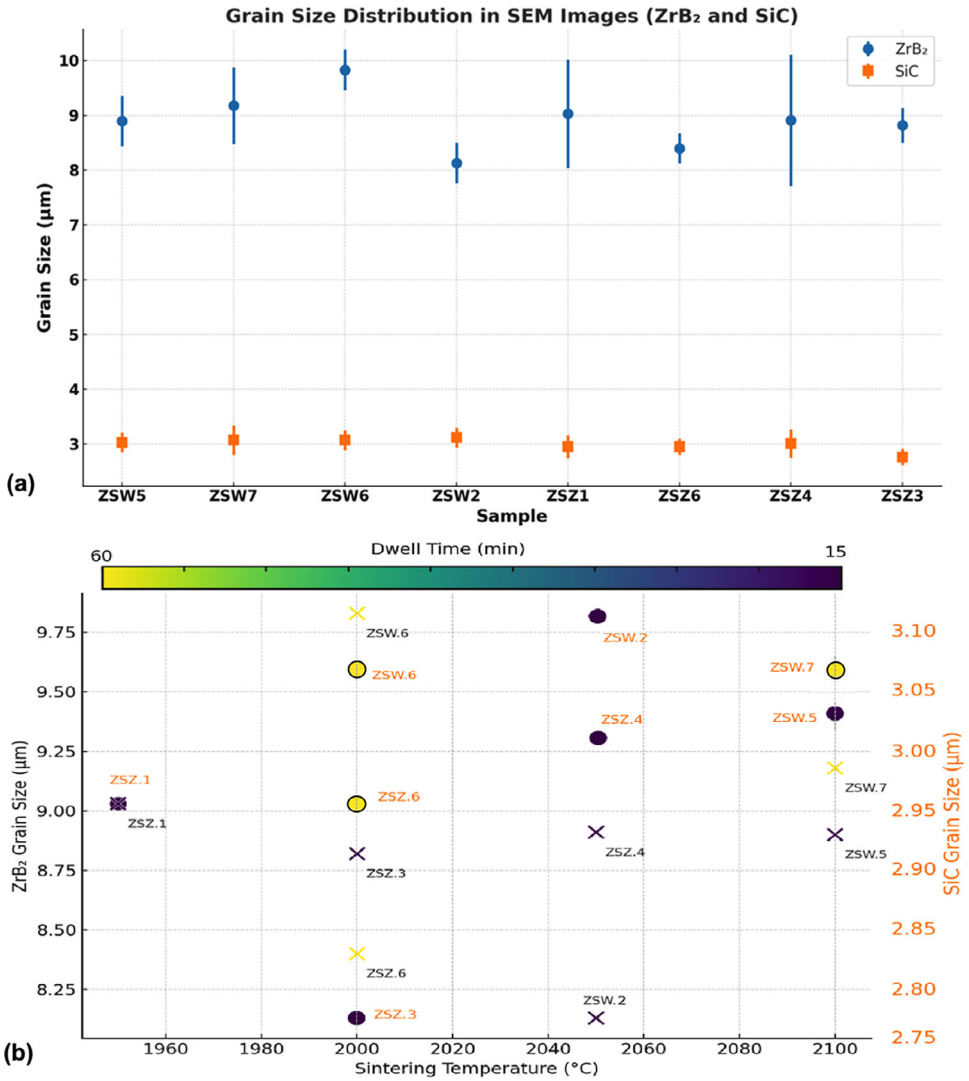

FIGURE 9 | (a) Sample-wise and (b) porosity-wise ZrB_2–SiC grain size distribution over the sintering temperature and dwell time.

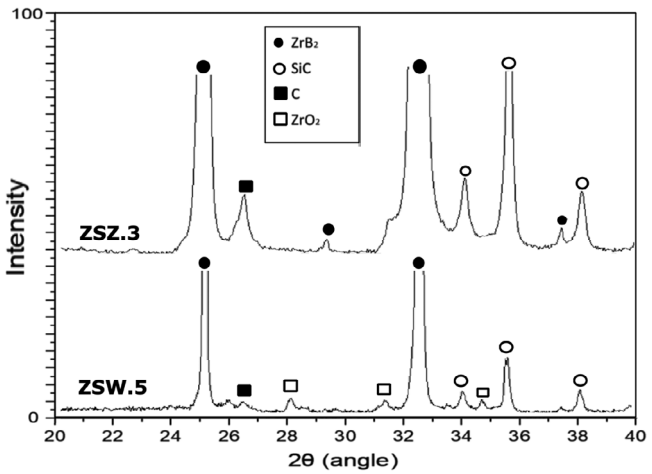

FIGURE 10 | XRD patterns of ZrB_2–SiC composites containing 20 mass% SiC for the least (ZSW.5) and most porous (ZSZ.3) sample.

porous ZrO_2-milled sample) and ZSW.5 (the densest WC-milled sample). Their diffraction patterns are shown in Figure 10. Both samples reveal ZrB_2 as the primary phase and SiC as the secondary phase, consistent with the nominal composition. However, a key difference emerges in the detection of ZrO_2 peaks, which is clearly present in ZSW.5 but absent in ZSZ.3. The ZrO_2 detected in ZSW.5 is likely a byproduct of localized oxidation during SPS, potentially aggravated by the use of WC milling media. High-energy ball milling can induce severe mechanical abrasion, leading to localized heating and surface activation. These conditions, combined with exposure to residual oxygen at grain boundaries or particle surfaces, may partially oxidize ZrB_2, forming ZrO_2. Additionally, cobalt present in WC balls may catalyze these reactions, especially at high sintering temperatures (≥2000°C).

In contrast, the ZrO_2-milled sample (ZSZ.3), despite being more porous, shows no detectable ZrO_2 in its XRD pattern. This absence suggests that ZrO_2 milling media is chemically more inert under the applied conditions and produces less mechanical abrasion, minimizing phase instability or compositional shifts. Additionally, since ZrO_2 is already present in the milling system, its presence in trace amounts might go undetected or be structurally indistinct from background noise unless significantly

TABLE 4 | Summary of results from this research, as obtained from open literature, illustrating the effect of different sintering parameters on densification and mechanical properties of ZrB_2–SiC composites.

SPS protocol (°C/MPa/min)	RD (%)	HV (GPa)	σ_f (MPa)	K_{IC} (MPa $m^{1/2}$)	References
1950/50/15	94.7	14.33	407	3.71	This work
2050/50/15	97.7	13.92	384	3.58	This work
2100/65/15	99.2	13.64	407	3.62	This work
2000/65/15	95.3	16.03	476	3.67	This work
2000/65/60	96.0	15.09	447	3.72	This work
2000/35/10	96.5	13.9	423	3.71	[25]
2000/30/10	97.2	15.4	—	4.50	[25]
1950/50/15	97.6	18.6	492	2.50	[26]
2000/32/–	—	16.3	231	—	[27]
1950/30/15	100.0	29.0	478	6.10	[28]
2000/32/–	—	—	425	—	[27]

incorporated. This distinction has direct implications for mechanical behavior. As shown earlier, ZSW.5, despite achieving the highest RD (99.2%), exhibited a moderate hardness of 13.64 GPa, while ZSZ.3, which was more porous (95.3%), displayed a higher hardness of 16.03 GPa. This contrast implies that the presence of ZrO_2 in ZSW.5, while not excessive, may slightly diminish hardness by introducing softer inclusions. However, it did not adversely affect σ_f or K_{IC}, indicating that its influence is subtle and likely confined to specific mechanical pathways.

These findings underscore that the milling medium plays a dual role. While WC aids densification and sintering kinetics, it also introduces reactive sites that can compromise phase purity. ZrO_2 milling, on the other hand, promotes chemical stability and phase integrity, though with a minor trade-off in densification efficiency. The selection of milling media should thus balance densification gains against potential chemical contamination, especially in systems where phase purity is critical.

3.5 | Comparative Analysis With Existing Literature

To benchmark the current results against the broader field, Table 4 presents a comparison with prior studies on ZrB_2–SiC composites processed under comparable SPS conditions (1950–2100°C, 30–65 MPa). The current work achieved relative densities ranging from 94.7 to 99.2%, which aligns well with the reported values of 96–100% in similar systems.

In terms of hardness, our samples achieved values between 13.64 and 16.03 GPa. While this range is modest compared with the highest values in literature (e.g., 29.0 GPa at 1950°C by Irom et al. [23]), it is important to consider the influence of starting particle size. The extreme hardness reported by Irom et al. is largely attributed to the use of nanosized starting powders, which facilitate Hall–Petch strengthening. In contrast, the present study utilized micron-sized powders (~5.5 μm ZrB_2), resulting in a coarser final grain structure but demonstrating what is achievable with commercially standard, cost-effective raw materials without sintering additives. σ_f values in this work range from 384 to 476 MPa, which is comparable to studies by Guo et al. [24] and Naughton-Duszova et al. [25], who reported strengths between 423 and 478 MPa. These outcomes reflect successful consolidation and microstructural cohesion in the present composites. K_{IC} values in this study (3.58–3.72 MPa $m^{1/2}$) also fall within the commonly reported range of 2.5–6.1 MPa $m^{1/2}$ [23, 25], although on the lower end due to the absence of interfacial engineering or crack deflection enhancements.

Notably, this study highlights that competitive densification and mechanical performance can be achieved through strategic selection of milling route and sintering parameters, even without chemical additives. For instance, the ZSW.5 sample matched or exceeded literature benchmarks in density and strength, while ZSZ.3 demonstrated exceptional hardness despite its porosity. These results confirm that balanced optimization of temperature, pressure, and dwell time, when combined with suitable milling, can yield reproducible, high-performance UHTCs.

Nevertheless, it should be noted that the absence of dopants limits the toughness enhancement potential. While transformation toughening or crack deflection mechanisms are more prominent in doped or nanoengineered systems, this work emphasizes scalable processing routes that maintain phase purity and achieve reliable performance.

4 | Conclusion

This study systematically explored how sintering temperature, pressure, and dwell time, across two distinct milling approaches, govern the densification, microstructure, and mechanical behavior of ZrB_2–20 vol% SiC UHTCs processed via SPS. Building upon earlier established sample series prepared using two milling routes (ZSW and ZSZ), this work systematically evaluates the effects of sintering conditions without the use of sintering

additives, aiming to optimize mechanical performance and microstructural stability.

Key conclusions drawn from the study are:

- Sintering temperature emerged as the dominant parameter, strongly promoting densification and grain growth. The highest RD (99.2%) was achieved in ZSW.5 (2100°C, 65 MPa, 15 min), while ZSZ samples peaked at 96.7%. Higher temperatures promoted densification but also accelerated grain coarsening, especially in ZrB_2.
- Dwell time and pressure had more subtle but critical effects. At 2000°C, extending the dwell time from 15 to 60 min enhanced both strength and densification without excessive grain coarsening. Pressure improvements plateaued beyond 50 MPa in already well-densified systems.
- Mechanical properties reflected these trends:
  - Flexural strength was highest (516 MPa) in ZSW.6, where high density and moderate grain size were achieved.
  - Hardness was highest (17.08 GPa) in fine-grained ZSZ.1 but declined with grain growth at higher temperatures.
  - Fracture toughness was relatively stable across samples but peaked in ZSZ compositions, which had finer grains and fewer secondary phases.
- Porosity ranking and grain size mapping confirmed that lower porosity strongly correlates with higher strength. The most porous sample (ZSZ.3, 4.7% porosity) exhibited intergranular voids and incomplete sintering, while the least porous (ZSW.5, 0.8% porosity) displayed compact grain structures with minimal defects.
- Grain size analysis showed that ZrB_2 grains grew with increasing temperature and dwell time (from ~8.1 to 9.8 μm), while SiC grain size remained relatively constant (~2.7–3.1 μm), acting as a grain growth inhibitor. Mechanical strength was maximized in samples with low porosity and moderate ZrB_2 grain size.
- Phase analysis via XRD revealed secondary ZrO_2 formation only in WC-milled (ZSW) samples, attributed to mechanochemical oxidation. This contamination reduced hardness slightly but did not compromise densification. Its presence underscores a trade-off between densification efficiency and chemical purity when selecting milling media.

Acknowledgments

This work is supported by Horizon Europe's research and innovation programme under the Marie Sklodowska-Curie grant agreement No. 101107214. The authors acknowledge the extensive support received from the Materials Science and Engineering section of the Faculty of Mechanical Engineering and Space System Engineering section of the Faculty of Aerospace Engineering, Delft University of Technology, the Netherlands.

References

1. J.-H. Yuan, Q.-Y. Liu, Y. You, et al., "Effect of ZrB_2 Powders on Densification, Microstructure, Mechanical Properties and Thermal Conductivity of ZrB_2-SiC Ceramics," *Ceramics International* 47 (2021): 15843–15848, https://doi.org/10.1016/j.ceramint.2021.02.158.

2. X. Chen, L. Trinh, Z. Hua, et al., "Microstructure, Mechanical, and Thermal Properties of Compositionally Complex (Hf,Zr,Nb,Ti)B_2 –LaB_6 Ceramics," *International Journal of Applied Ceramic Technology* (2025), https://doi.org/10.1111/ijac.70068.

3. J. Meng, H. Fang, H. Wang, et al., "Effects of Refractory Metal Additives on Diboride-based Ultra-high Temperature Ceramics: A Review," *International Journal of Applied Ceramic Technology* 20 (2023): 1350–1370, https://doi.org/10.1111/ijac.14336.

4. I. Akin, M. Hotta, F. C. Sahin, O. Yucel, G. Goller, and T. Goto, "Microstructure and Densification of ZrB_2–SiC Composites Prepared by Spark Plasma Sintering," *Journal of the European Ceramic Society* 29 (2009): 2379–2385, https://doi.org/10.1016/j.jeurceramsoc.2009.01.011.

5. D. Sciti, A. Vinci, L. Zoli, et al., "Propulsion Tests on Ultra-high-temperature Ceramic Matrix Composites for Reusable Rocket Nozzles," *Journal of Advanced Ceramics* 12 (2023): 1345–1360, https://doi.org/10.26599/JAC.2023.9220759.

6. F. Monteverde and A. Bellosi, "Microstructure and Properties of an HfB_2-SiC Composite for Ultra High Temperature Applications," *Advanced Engineering Materials* 6 (2004): 331–336, https://doi.org/10.1002/adem.200400016.

7. I. Krinis, P. Jindal, V. Popovich, H. Brouwer, J. Botchu, and Y. Tang, "Optimizing Densification and Mechanical Properties of Spark Plasma Sintered ZrB_2-SiC Ceramic Composites," *Ceramics International* 51 (2025): 41877–41890, https://doi.org/10.1016/J.CERAMINT.2025.06.408.

8. Test Method for Water Absorption, Bulk Density, Apparent Porosity, and Apparent Specific Gravity of Fired Whiteware Products, Ceramic Tiles, and Glass Tiles, https://doi.org/10.1520/c0373-88r06.

9. Test Methods for Determining Average Grain Size, https://doi.org/10.1520/e0112-13r21.

10. Z. Ihsani, Porosity Analysis Procedure With ImageJ, https://www.academia.edu/24152953/Porosity_Analysis_Procedure_with_ImageJ.

11. F. Monticeli, H. Voorwald, and M. O. Cioffi, "Porosity Measurement in Carbon-Fiber-Reinforced Polymer Composite through Optical Microscopy Using ImageJ Software," in *Advances in Mechanical and Power Engineering*, ed. Altenbach H., Cheng A.H.-D., Gao X.-W., Kostikov A., Kryllowicz W., and Lampart P., (Springer International Publishing, 2023), 265–273, https://doi.org/10.1007/978-3-031-18487-1_27.

12. N. Hojat, P. Gentile, A. M. Ferreira, and L. Šiller, "Automatic Pore Size Measurements From Scanning Electron Microscopy Images of Porous Scaffolds," *Journal of Porous Materials* 30 (2023): 93–101, https://doi.org/10.1007/s10934-022-01309-y.

13. Test Method for Vickers Indentation Hardness of Advanced Ceramics, https://doi.org/10.1520/c1327-08.

14. Test Method for Flexural Strength of Advanced Ceramics at Ambient Temperature, https://doi.org/10.1520/c1161-13.

15. C. B. Ponton and R. D. Rawlings, "Vickers Indentation Fracture Toughness Test Part 1 Review of Literature and Formulation of Standardised Indentation Toughness Equations," *Materials Science and Technology* 5 (1989): 865–872, https://doi.org/10.1179/mst.1989.5.9.865.

16. B. R. Lawn and M. V. Swain, "Microfracture beneath Point Indentations in Brittle Solids," *Journal of Materials Science* 10 (1975): 113–122, https://doi.org/10.1007/BF00541038.

17. G. D. Quinn and R. C. Bradt, "On the Vickers Indentation Fracture Toughness Test," *Journal of the American Ceramic Society* 90 (2007): 673–680, https://doi.org/10.1111/j.1551-2916.2006.01482.x.

18. H. Fischer, "Fracture Toughness of Dental Ceramics: Comparison of Bending and Indentation Method," *Dental Materials* 18 (2002): 12–19, https://doi.org/10.1016/S0109-5641(01)00005-7.

19. W. G. Fahrenholtz and G. E. Hilmas, "Ultra-high Temperature Ceramics: Materials for Extreme Environments," *Scripta Materialia* 129 (2017): 94–99, https://doi.org/10.1016/j.scriptamat.2016.10.018.

20. S. C. Zhang, G. E. Hilmas, and W. G. Fahrenholtz, "Mechanical Properties of Sintered ZrB_2–SiC Ceramics," *Journal of the European Ceramic Society* 31 (2011): 893–901, https://doi.org/10.1016/j.jeurceramsoc.2010.11.013.

21. J. Zou, G. Zhang, C. Hu, et al., "Strong ZrB_2–SiC–WC Ceramics at 1600 C," *Journal of the American Ceramic Society* 95 (2012): 874–878, https://doi.org/10.1111/j.1551-2916.2011.05062.x.

22. A. L. Chamberlain, W. G. Fahrenholtz, G. E. Hilmas, and D. T. Ellerby, "High-strength Zirconium Diboride-based Ceramics," *Journal of the American Ceramic Society* 87 (2004): 1170–1172, https://doi.org/10.1111/j.1551-2916.2004.01170.x.

23. E. Irom, M. Zakeri, M. Razavi, and M. Farvizi, "ZrB_2 -based Ultrahigh-temperature Ceramic With Various SiC Particle Size: Microstructure, Thermodynamical Behavior, and Mechanical Properties," *International Journal of Applied Ceramic Technology* 22 (2025): e14855, https://doi.org/10.1111/ijac.14855.

24. Q. L. Guo, J. G. Li, Q. Shen, and L. M. Zhang, "Effect of High-Energy Ball Milling of ZrB_2 Powder on the Microstructure and Mechanical Properties of ZrB_2-SiC Ceramics," *Key Engineering Materials* 512–515 (2012): 723–728, https://doi.org/10.4028/www.scientific.net/KEM.512-515.723.

25. A. Naughton-Duszova, E. Bączek, and M. Podsiadło, "Selected Properties of ZrB_2 Composites Obtained by SPS Method for Parts of Electro-erosion Shaping Machines," *Mechanik* (2018): 155–158, https://doi.org/10.17814/mechanik.2018.2.32.

26. R. Stadelmann, (2013), Mechanical properties and thermal residual stresses of ZrB_2-SiC ceramic composites for hypersonic vehicle applications.

27. N. Seetala, C. L. Prevo, L. E. Matson, T. S. Key, and I. I. Park, "Spark Plasma Sintering of High-Energy Ball-Milled ZrB_2 and HfB_2 Powders With 20vol% SiC," *Materials Science Forum* 941 (2018): 1990–1995, https://doi.org/10.4028/www.scientific.net/MSF.941.1990.

28. R. Hassan and K. Balani, "Densification Mechanism of Spark Plasma Sintered ZrB_2 and ZrB_2-SiC Ceramic Composites," *Materials Characterization* 179 (2021): 111320, https://doi.org/10.1016/j.matchar.2021.111320.